

Investigating Twin Star Equation of States in Light of Recent Astrophysical Observations

Shamim Haque , ^{*} Atharva Shinde , [†] Asim Kumar Saha , [‡] Tuhin Malik , [§] and Ritam Mallick , [¶]

¹*Indian Institute of Science Education and Research Bhopal, Bhopal 462066, India*

²*Departamento de Física, Universidade de Coimbra, 3004-516 Coimbra, Portugal*

(Dated: January 26, 2026)

Twin stars are predicted to exist in nature if the hadron-to-quark phase transition is strong enough to form a new branch of hybrid stars, separated from the branch of neutron stars. It is essential to study the hybrid equations of state that can form twin stars, with a primary focus on estimating the onset of phase transition and its strength. We adopt an agnostic approach, using transition energy density, transition pressure, the discontinuity strength, and a constant speed of sound for quark matter as our parameter space to construct a large possibility of hybrid equations of state, and thereby encapsulating a comprehensive picture of the twin star scenario. First we report the complete conditions on our parameter space imposed by the general relativistic hydrostatic equilibrium solutions. For a fixed transition energy density and speed of sound for quark matter, we define distinct ranges of transition pressures based on the allowed strengths of discontinuity. Below a maximum transition pressure, a range of discontinuity exists that increases as the transition pressure decreases. Thereby, we identify the loci of the limits on discontinuities as the ‘witch-hat’ curves. Based on the causality limit, the witch-hat curves can be punctured or incomplete. Strong constraints on this picture are drawn from the inferences from GW170817 and the NICER measurements, especially from the recent measurements of PSR J0614–3329 and PSR J0437–4715, which point towards a softer equation of state around the canonical mass of neutron stars. We computed the maximum mass for twin stars to be $2.05 M_{\odot}$, the allowed strongest discontinuity in rest-mass density to be $7.76\rho_{\text{sat}}$, and the upper bound on transition rest-mass density to be $4.03\rho_{\text{sat}}$. Subsequently, we compute the implications of the stiffness of the quark matter equation of state on this picture. Different confidence levels for observational inferences are considered to assess the extent of inclusion (and rejection) of hybrid equations of state and, consequently, their effects on the limits of the maximum mass of twin stars, the maximum transition density and the allowed strongest discontinuity.

I. INTRODUCTION

The pursuit of understanding the equation of state (EoS) of matter inside a Neutron Star (NS) is a traditional one [1–3]. It remains an important revisit as we continue to observe more of the universe with increasingly advanced technologies, particularly by measuring these compact objects and witnessing the violent events involving them. NSs possess strong gravity such that the matter at the core is compressed beyond nuclear saturation density $\rho_{\text{sat}} \simeq 2.7 \times 10^{14} \text{ g/cm}^3$ [4]. The unavailability of such circumstances on earth-based environments makes NSs the natural laboratories in the universe to study the behaviour of matter at low temperatures and high densities [5–8]. At such extreme conditions, a phase transition (PT) from hadronic matter (HM) to quark matter (QM) is expected from Quantum Chromodynamics (QCD) [9].

The objective to achieve an integrated picture of QCD has been approached from various directions. In the principles of Chiral Effective Field Theory [10–14], the EoS

of the cold matter is well-anticipated to be in hadronic state upto $\sim 1.1\rho_{\text{sat}}$ [15–22]. From the earth-based experiments involving the relativistic heavy-ion collision has mainly probed the EoS of matter at high temperatures and low densities [23–27]. Theoretical framework of lattice QCD [28–30] efficiently probes the matter at low densities, however, interfered by sign problem [31, 32] when extended to densities at the regimes of NSs. Perturbative QCD (pQCD) calculations [33–44] have computed on behaviour of matter asymptotically high densities ($\sim 40\rho_{\text{sat}}$).

To probe the density regime that resides inside the core of an NS ($1 \sim 10 \rho_{\text{sat}}$), there are a couple of directions to move forward. Strong constraints have been drawn from the precise mass-radius measurements made by the NICER X-ray observations [45–53]. Importantly, the recent mass-radius measurement of PSR J0614–3329 [52] and PSR J0437–4715 [53] point towards a softer EoS, in contrast to the earlier measurements of J0030+0451 [45–47] and J0740+6620 [48–51], which suggested otherwise. Additional assistance came from the multi-messenger astronomy, mainly the observation of gravitational waves from binary merger of NSs [54], which has inferred constraints on the tidal deformability of NSs [55–60], which also steers the investigation to a softer composition of matter around the canonical mass of NS ($1.4 M_{\odot}$). On the other side, the mass measurement of massive pulsars ($\gtrsim 2.0 M_{\odot}$) [61–65] advocate for a relatively stiffer EoS.

^{*} Contributed equally, shamims@iiserb.ac.in

[†] Contributed equally, atharva21@iiserb.ac.in

[‡] asim21@iiserb.ac.in

[§] tuhin.malik@uc.pt

[¶] mallick@iiserb.ac.in

Despite the progress made, there can still exist a plethora of thermodynamically consistent EoSs that comply with the observational status discussed above [66–70]. The attempts to probe the properties of PT remain important yet inadequate. Primarily, the onset of PT is not known *a priori*, and the nature of first-order PT is proposed by models that include—(i) Maxwell construction—the PT is modelled as a transition using discontinuity jump in the density at a constant pressure, (ii) Gibbs construction—the HM and QM coexist in a mixed phase inside a region of pressure-density [71, 72]. With such prospects and uncertainties in hand, model-agnostic approaches are useful for encapsulating all possibilities in an EoS describing the behaviour of matter inside NSs [70, 73–76].

A typical hybrid EoS with Maxwell-type PT constructed out of an agnostic approach consists of a pure hadronic part at lower densities and a pure quark part at higher densities separated by a PT region described by a discontinuous jump in the density at constant transition pressure. Under the general relativistic hydrostatic equilibrium conditions governed by the Tolman Oppenheimer Volkoff (TOV) equations [77, 78], such EoSs indicate the existence of hybrid stars (HSs), which contain a quark seed within a hadronic shell. Interestingly, within the constraints imposed by astrophysical observations, the discontinuity in the density jump that describes the strength of the PT can be large enough to give rise to a third branch of HSs, separated from the second branch of NSs [79, 80]. In this context, the first branch of compact objects refers to the family of white dwarfs. Such scenarios form the twin stars (TSs) that reside on the third branch (smaller radius, more compact) but have equal mass with respect to NSs on the second branch (larger radius, less compact).

TSs are the direct manifestation of strong hadron-to-quark PT. Observation of such candidates of compact objects can confirm the occurrence of PT in the astrophysical scenarios and severely constrain the EoS [66, 81–94], especially if detections are made in the high-mass regime [95–98]. On the other hand, the formation of TSs in realistic scenarios and their dynamical evolution remain a serious pursuit [99, 100]. Several studies have presented the possibility of realistic EoSs that can construct such species [81, 101–112]. A few works have studied the oscillation modes [113–117], QCD trace anomaly [118], rotation [119–122], magnetic fields [123, 124] and temperature effects [125–127] on these compact objects.

En route to uncovering the TS scenario, it is essential to sketch a comprehensive (if not the complete) picture of TSs, considering the large possibility of hybrid EoSs that can coexist with recent observational constraints. In this study, we adopt an agnostic approach to build an ensemble of EoSs that can capture TS solutions. In particular, we allow transition energy density and transition pressure to vary freely to allow a larger set of hadronic EoSs within the causality limit to form hybrid EoSs. Systematic analysis of such an inclusive set of EoSs reveals

more of the TS scenario presented in the previous literature. We revisit the criteria for TS solutions as given by the TOV equations to gain a comprehensive picture beyond the existing literature. In particular, we define the ‘witch-hat’ curves for a choice of transition energy density and stiffness of quark matter EoS. The effects of causality and the properties of PT on these curves are exhaustively addressed, revealing specific conditions that can give rise to punctured or incomplete witch-hat curves. Previous studies have constructed witch-hat like curves only for a limited or fixed hadronic EoS [79, 80, 83]. After establishing the framework under hydrostatic equilibrium within the limits of causality, we constrain the picture using recent observational inferences and set bounds on the properties of PT and the maximum mass of TSs. In particular, the recent inferences from PSR J0614–3329 and PSR J0437–4715 are rather strong and constitute an important constraint to be included in new studies.

The article is organized in the following way. In Sec. II, we discuss the agnostic approach adopted to construct the ensemble of hybrid EoS, define our parameter space, and outline our strategy for locating the third branch. In Sec. III, we discuss our results in three main parts—approach from TOV, constraints from observation and possible bounds on the TS scenario. Finally, we conclude our work with remarks in Sec. IV.

II. FORMALISM

A. Equation of State

We employ an agnostic approach to systematically construct EoSs that provide a macroscopic description of matter properties, particularly the connection between the thermodynamic quantities—rest-mass density (ρ), energy density (e), and pressure (P). The EoSs are computed using the following parameters:

- *transition energy density (e_{tr})*
- *transition pressure (P_{tr})*
- *discontinuity in energy density (Δe)*
- *constant speed of sound for quark EoS ($c_{s,\text{QM}}^2$)*

The independent choices of e_{tr} and P_{tr} decide the stiffness of hadronic EoS. These parameters are sufficient to describe hybrid EoSs with first-order PT, which mainly involves large discontinuities. We recall that TSs have been categorised based on the maximum mass of the second branch ($M_{\text{TOV},2}$) and the third branch ($M_{\text{TOV},3}$) in Ref. [80], which are as follows:

- *Category I:* $M_{\text{TOV},2} \geq 2.0 M_{\odot}$ and $M_{\text{TOV},3} \geq 2.0 M_{\odot}$, particularly associated with higher e_{tr} .
- *Category II:* $M_{\text{TOV},2} \geq 2.0 M_{\odot}$ and $M_{\text{TOV},3} \leq 2.0 M_{\odot}$, particularly associated with larger Δe .

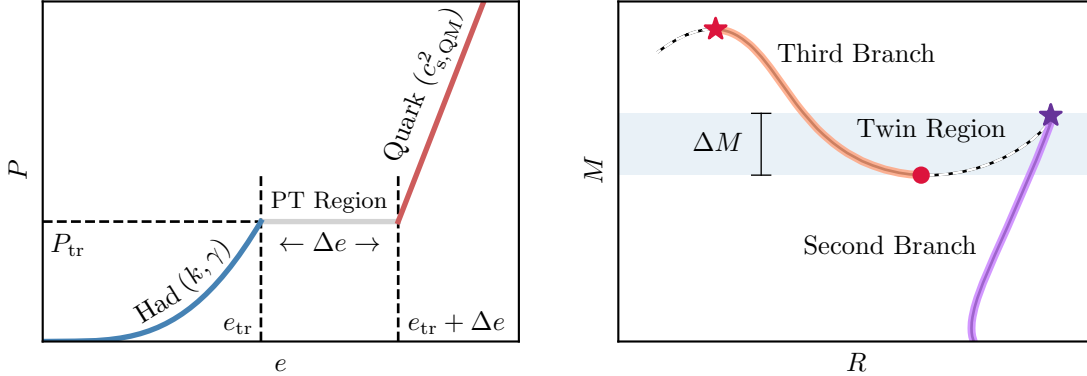


FIG. 1. [Left] Diagram indicating the different parts of EoS, that are controlled by different parameters—transition energy density (e_{tr}), transition pressure (P_{tr}), the strength of discontinuity in energy density (Δe) and constant speed of sound for quark matter EoS ($c_{s,\text{QM}}^2$). [Right] Schematic diagram of M – R sequence of an EoS that constructs TSs. The second (purple) and third (orange) stable branches are separated by a sequence of unstable branch (black dashed curve). The maximum mass on the second and third branches ($M_{\text{TOV},2}$ and $M_{\text{TOV},3}$) is indicated by purple and red stars, respectively. The sequence of unstable stars begins beyond these stellar configurations. The minimum mass on the third branch is indicated by a red circle. The twin region is defined as the mass range in which equal-mass stellar models are present on both stable branches.

- *Category III:* $M_{\text{TOV},2} \leq 2.0 M_{\odot}$ and $M_{\text{TOV},3} \geq 2.0 M_{\odot}$.
- *Category IV:* $M_{\text{TOV},2} \leq 1.0 M_{\odot}$ and $M_{\text{TOV},3} \leq 2.0 M_{\odot}$, particularly associated with low P_{tr} .

See Fig. 3 in Ref. [83] for schematic reference. Each EoS is set up using the four sections explained below:

- *Crust Region:* At smaller densities ($\lesssim 0.4\rho_{\text{sat}}$), a fixed crust EoS is built using four piecewise polytropes, which are taken from Table II in Ref. [74]. The addition of this part remains common throughout all the EoSs constructed for this study.
- *Hadronic Region ($e < e_{\text{tr}}$):* An additional polytrope is added above the crust EoS to mimic the hadronic matter, with adiabatic index γ as a free parameter. The thermodynamic quantities— P and e are given in terms of ρ as,

$$P(\rho) = k\rho^\gamma, \quad e(\rho) = \rho(a+1) + \frac{P}{\gamma-1} \quad (1)$$

The polytropic constant (k) and a are computed using the boundary condition to ensure continuity of $P(\rho)$ and $e(\rho)$ between the crust and the hadronic EoS. The independent choices for e_{tr} and P_{tr} allow for finding an appropriate value of γ and transition rest-mass density (ρ_{tr}). These quantities are numerically computed using the equations,

$$\rho_{\text{tr}} = \left(\frac{P_{\text{tr}}}{k} \right)^{1/\gamma}, \quad e_{\text{tr}} = \rho_{\text{tr}}(1+a) + \frac{P_{\text{tr}}}{\gamma-1} \quad (2)$$

For a fixed e_{tr} , a higher (lower) value of P_{tr} will set a higher (lower) value of γ , resulting in a stiffer (softer) hadronic EoS.

- *Phase Transition Region ($e_{\text{tr}} < e < e_{\text{tr}} + \Delta e$):* The PT region is computed after fixing e_{tr} and P_{tr} , allowing a free choice to be made for Δe . This value decides the strength of the discontinuity of PT. The pressure will remain constant in this region as given by P_{tr} . This step leads to the construction of Maxwell-type PT [72]. Since the chemical potential remains constant in the region of PT, the $\Delta\rho$ can be computed as,

$$\Delta\rho = \frac{\rho_{\text{tr}}\Delta e}{P_{\text{tr}} + e_{\text{tr}}} \quad (3)$$

- *Quark Region ($e > e_{\text{tr}} + \Delta e$):* The quark part is modelled using the constant speed of sound (CSS) parametrisation with $c_{s,\text{QM}}^2$ [79, 80]. The pressure in the quark region is given as,

$$P(e) = P_{\text{tr}} + c_{s,\text{QM}}^2 e \quad (4)$$

Fig 1 (left) shows the schematic diagram of the EoS construction method described above. First, we fix a value of e_{tr} , after which the P_{tr} can be varied from an upper bound set by the limit of causality, that is, the maximum value of P_{tr} is set at a value where $c_s^2(P_{\text{tr}}, e_{\text{tr}}) = 1$. However, if the central pressure of M_{TOV} of hadronic EoS is smaller than this upper limit of pressure, then the maximum value of P_{tr} is set to the central pressure of the stellar configuration at M_{TOV} . This rule assures that we induce PT in the relevant positions of an M – R sequence and not in the cores of unstable stellar models beyond M_{TOV} .

On the other hand, the lower limit of P_{tr} is set to a value where such a central pressure would construct an NS of $1 M_{\odot}$, which means $M_{\text{TOV},2} > 1 M_{\odot}$. However, if an unstable branch is formed by an EoS that constructs

$M_{\text{TOV},2} = 1 M_{\odot}$, we only increase Δe up to a limit where the third branch forms a minimum mass up to $0.7 M_{\odot}$. We do not construct EoSs which form a minimum mass below $0.7 M_{\odot}$ in the third branch. These choices are made to restrict our search to reasonable PT densities. In theory, such EoS (with large Δe and very small P_{tr}) can be constructed where TSs can form at very low masses ($\lesssim 0.5 M_{\odot}$), which are far from the NS range (minimum mass of NSs is known to be $\sim 1.1 M_{\odot}$ [128, 129]). Searches for such TS solutions are avoided in this study. Whereby, we do not survey the TSs of category IV, which are not responsible for constructing massive TSs or assisting in setting upper limits on the e_{tr} and Δe . Moreover, small P_{tr} at large e_{tr} will make extremely soft hadronic EoSs, resulting in hybrid EoSs that will be unable to support massive NSs ($\gtrsim 2.0 M_{\odot}$). Hence, we find TSs of category IV will be strictly ruled out at large e_{tr} . At lower e_{tr} , the acceptance of such TSs can be anticipated from our analysis and does not require specific exploration. See Refs. [80, 102, 103, 107, 111], which have especially examined TSs of category IV.

For the PT region, the minimum e_{tr} (ρ_{tr}) used in this study is $3 \times 10^{14} \text{ g/cm}^3$ ($\approx 1 \rho_{\text{sat}}$). The CET sufficiently predicts that matter resides as hadronic matter up to $\sim 1.1 \rho_{\text{sat}}$ [130, 131]. We construct a bunch of hadronic EoSs by uniformly varying P_{tr} in the described range and set the quark matter EoS on the other side by fixing a value for $c_{s,\text{QM}}^2$. The Δe (and hence $\Delta \rho$) is adaptively varied to find the limits on its allowed range, such that the given pair of hadronic and quark EoS can construct TS solutions. The accuracy of determining the limits on Δe ($\Delta \rho$) is considered up to 10^{12} g/cm^3 ($\approx 10^{-2} \rho_{\text{sat}}$).

B. Locating third branch

Fig. 1 (right) shows the schematic diagram of the M – R sequence that has separated second and third branches containing TSs. To detect the TS solutions in the third branch, we first locate the central density of the maximum mass configuration on the second branch (purple curve), which is constructed from the hadronic EoS. Based on the Seidov criteria [132], upon increasing the central density to build further stellar models, the EoS may allow for two scenarios. The immediate sequence of HSs may continue to be in the second branch, or they may fall into the unstable branch (discussed as scenarios (b) and (d) in Fig. 2 of reference [79]). In either of the situations, the $M_{\text{TOV},2}$ is computed as indicated with a purple star in Fig. 1 (right). Consequently, an unstable branch (black dashed curve) is recognised only if the mass of the subsequent stellar models decreases up to $\Delta M = 10^{-3} M_{\odot}$ with respect to the purple star. The quark EoS can be stiff enough that a third branch (orange curve) may appear after a sequence of unstable HSs. The third branch is detected only if the mass of the subsequent stellar models increases up to $\Delta M = 10^{-3} M_{\odot}$ from the minimum mass in the unstable branch (indi-

cated with a red circle). Finally, the third branch reaches its $M_{\text{TOV},3}$ (indicated with a red star), and the subsequent stellar models form another unstable branch (black dashed curve). Once we numerically obtain this sequence of branches within the tolerance ΔM , the EoS is recognised to have produced TS solutions.

The detection margin of $\Delta M = 10^{-3} M_{\odot}$ is suitable for our study, as this accuracy is several orders of magnitude above the observational accuracy [45, 49, 51–53, 61–65, 133–137]. Besides, detection margins $\Delta M < 10^{-3} M_{\odot}$ lead to ambiguity between the physical stable/unstable branches versus a local fluctuation due to numerical calculation, which are highly probable when TOV equations have to handle EoSs with strong and discontinuous PT.

III. RESULTS

We discuss the results from two main perspectives. Within the described parameter space, we analyse the conditions on allowed EoSs that give rise to the TS scenario, purely governed by TOV solutions. Based on the established theoretical framework, we apply recent observational constraints to further develop inferences, including upper bounds on transition densities, the strength of the PT discontinuity, and the maximum mass of TSs.

A. Inferences from TOV solutions

Fig. 2 shows a schematic picture of the region in EoS space with a fixed e_{tr} , indicating the allowed region of Δe that can form TSs. The grey region indicates the range of hadronic EoSs constructed according to the fixed e_{tr} and the allowed range of P_{tr} set by our formalism. By varying the P_{tr} in this range and fixing a value for $c_{s,\text{QM}}^2$, we identify three distinct regions based on the allowed conditions on Δe , which are explained below.

Solution-less Region (Red)—In this region, TSs do not form for any value of Δe , as shown in Fig. 2 (left panel). The inset shows the M – R sequences of selected EoSs that have P_{tr} in this region, emphasising that a third branch does not appear in these sequences after entering the unstable branch beyond $M_{\text{TOV},2}$. For such combinations of e_{tr} and P_{tr} , the quark EoS is not stiff enough to form another stable branch beyond the unstable branch.

Bound Region (Blue)—The maximum value of P_{tr} in this region (indicated as $P_{\text{tr}}^{\text{max}}$) is extracted numerically, at which TSs can form for a unique value of Δe . For $P_{\text{tr}} < P_{\text{tr}}^{\text{max}}$, there exists a range of Δe , in which TSs can form, as shown in Fig. 2 (middle panel). We selected three EoSs in this region, two of which lie outside the allowed region of Δe . The inset showing the respective M – R sequences indicates that only the EoS having Δe within the allowed region forms a third branch beyond the second branch, which is separated by an unstable branch. The sequence of TSs is indicated by the cyan

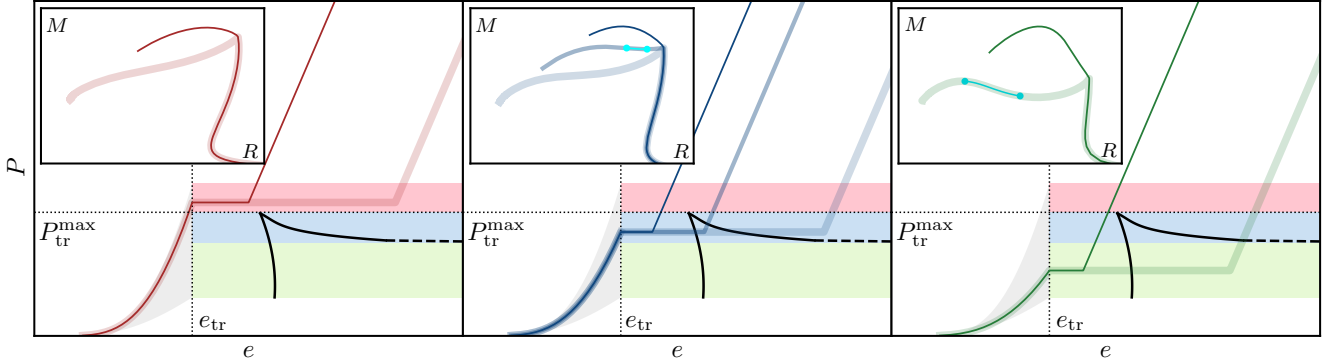


FIG. 2. Allowed region of EoS space with fixed e_{tr} that allows TS solutions. The grey region indicates the range of hadronic EoS considered in constructing the hybrid EoSs. The *solution-less region* (red) indicates the range of P_{tr} inside which TSs do not form. The left panel shows the M – R sequences of two EoSs in this region with different Δe . The *bound region* (blue) is separated from the red region using P_{tr}^{\max} at which a Δe exists that allows TS solutions. The middle panels show that the EoS with Δe within the allowed values of Δe constructs TSs. The sequence of the TSs is indicated by cyan in the inset. The *unbound region* (green) region only contains the minimum value of Δe above which TS solutions are possible. The right panel shows that the EoS with large value of Δe form TSs. The sequence of TSs is indicated by turquoise in the inset. The loci of minimum and maximum Δe are indicated in black, which we identify as the ‘witch-hat’ curve. The black dashed line is an extrapolation of the maximum Δe .

curve on the third branch. Decreasing P_{tr} results in an increase in the maximum limit of Δe and thereby increasing the range of Δe allowed for TS solutions. At the lowest value of P_{tr} in this region, the maximum limit of Δe is no more found in our numerical setup. However, an extrapolation using the locus of maximum Δe in this region indicates the growing (rather blowing up) nature of maximum Δe for the smaller values of P_{tr} .

Unbound Region (Green)—This region contains only a minimum value of Δe , as there is no maximum limit on Δe . As shown in Fig. 2 (right), we selected two EoSs from either side of the minimum Δe . The respective M – R sequences show that TSs (indicated by the turquoise curve on the third branch) can form for much larger values of Δe . The plot shows the end of this region at a minimum value of P_{tr} , where $M_{\text{TOV},2} = 1 M_{\odot}$. However, that is only a restriction applied to the EoS survey in this study. The formation of TSs is still possible below the minimum value of P_{tr} accounted in this study. That is, the locus of minimum Δe will continue to exist below the limit of this region.

In this article, we identify the loci of minimum and maximum Δe with varying P_{tr} and fixed e_{tr} as the ‘witch-hat’ curve (because the set of loci resembles a witch’s hat) to simplify the discussion around this picture. We note that a witch-hat curve can be computed for a given combination of the parameters— $(e_{\text{tr}}, c_{s,\text{QM}}^2)$. A point under the witch-hat curve represents a unique EoS (informing the values of P_{tr} and Δe in addition to e_{tr} and $c_{s,\text{QM}}^2$) that constructs TS solutions. Similar curves have been discussed before in the literature, but with a fixed hadronic EoS, which constrains P_{tr} given the choice of e_{tr} [79, 80]. While treating P_{tr} and e_{tr} as free variables, we are able to explore a larger possibility of EoS, resulting

in new features about the witch-hat curve that have not been discussed previously.

In Fig. 3 (left), we show that the witch-hat curves heavily depend on the variation in $(e_{\text{tr}}, c_{s,\text{QM}}^2)$. We find that an increase in e_{tr} leads to an increment in the size of the witch-hat curve, indicating a larger region is allowed for P_{tr} and Δe . For a fixed e_{tr} , the lower values of $c_{s,\text{QM}}^2$ form a smaller witch-hat with a lower value of P_{tr}^{\max} . Interestingly, we observe a puncture on the tip of the witch-hat curve formed by $(e_{\text{tr},b}, c_{s,\text{QM}1}^2)$. Here, the loci of the minimum and maximum of Δe do not meet, which is different from the expected picture discussed in Fig. 2. We find that for such a case, the P_{tr}^{\max} would be beyond the causality limit, which is also the upper limit for the survey range of P_{tr} . If we were to allow a survey of hadronic EoSs beyond the causality limit, the witch-hat curve would have been completed. As we lower the value of e_{tr} , for instance $(e_{\text{tr},a}, c_{s,\text{QM}1}^2)$, we find that the witch-hat curve is even more incomplete, where we only find the locus of minimum Δe . Such scenarios result in P_{tr} at the causality limit to be present in the unbound region (green) of Fig. 2, and hence the incomplete witch-hat curve would not have a well-defined bound region (blue). Hence, for the incomplete witch-hat curves, we define P_{tr}^{\max} at the causality limit. However, for smaller values of $c_{s,\text{QM}}^2$, the witch-hat curve can be complete. For example, the witch-hat curve for $(e_{\text{tr},b}, c_{s,\text{QM}2}^2)$ is complete, whereas the witch-hat curve for $(e_{\text{tr},b}, c_{s,\text{QM}1}^2)$ is punctured. This effect is expected from the fact that smaller $c_{s,\text{QM}}^2$ forms the witch-hat curve in the lower range of P_{tr} .

In Fig. 3 (right), we compute the witch-hat curves in $\Delta e/e_{\text{tr}} - P_{\text{tr}}/e_{\text{tr}}$ axis plot, which has been majorly used to study this subject in the past literature [79, 80]. Since the Seidov lines align in this plot, unlike in Fig. 3 (left),

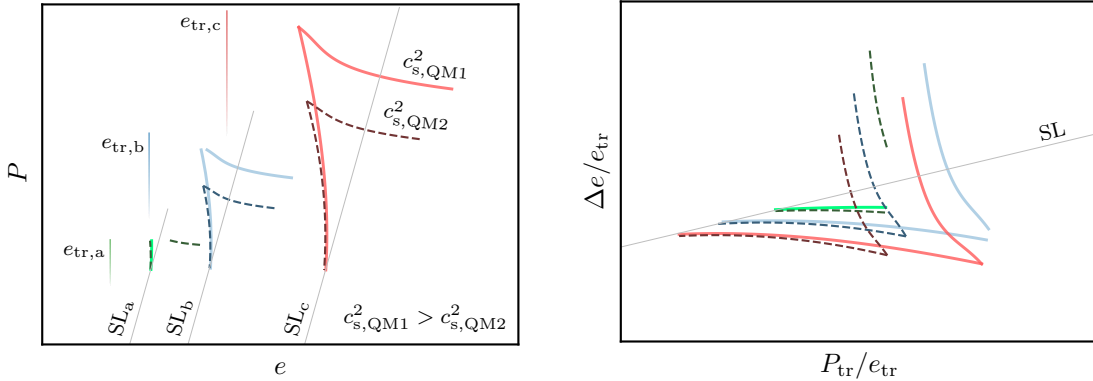


FIG. 3. The effects of change in e_{tr} and $c_{s,QM}^2$ on witch-hat curve. [Left] The vertical fading lines indicate the e_{tr} . The respective Seidov lines of each e_{tr} are indicated in grey solid lines. [Right] The Seidov lines align in the modified axes.

the effect of e_{tr} and $c_{s,QM}^2$ on witch-hat curves can be compared directly. We demonstrate that the picture surrounding the witch-hat curves discussed in this study agrees with the special cases presented in earlier studies. Therefore, the bifurcation of the region under the witch-hat curve based on categories of TSs, as defined in Ref. [80] (see Fig. 6 therein), remains consistent and applicable in our work.

We observed that the TOV solutions can put only an upper limit on P_{tr} (if not by the causality limit). No upper limit is provided for the e_{tr} or Δe (at small values of P_{tr}). Interestingly, we find that the current conglomerate of the observational measurements can provide strong constraints on this picture, including an upper bound for e_{tr} and appropriate limits on Δe .

B. Constraints from recent observational measurements

For developing further constraints from astrophysical point of view, we incorporated observational inference from NICER mass-radius measurements (PSR J0614-3329 [52], PSR J0437-4715 [53], PSR J0030+0451 [45-47], and PSR J0740+6620 [48-51]), the mass measurement of massive pulsar PSR J0348+0432 [63], and the tidal deformability from GW170817 [60]. Fig. 4 shows that the allowed region under a witch-hat curve can be heavily constrained using these observational constraints (using 2σ confidence), and only selective regions of $(P_{tr}, \Delta e)$ are allowed for each value of e_{tr} . We present this picture using three specific values of e_{tr} (with $c_{s,QM}^2 = 1.0$), which sufficiently explain the constraints received from observational measurements at different regimes of transition densities:

- *small*: $e_{tr} = 3 \times 10^{14} \text{ g/cm}^3$, $\rho_{tr} \approx 1\rho_{sat}$
- *intermediate*: $e_{tr} = 6 \times 10^{14} \text{ g/cm}^3$, $\rho_{tr} \approx 2\rho_{sat}$
- *large*: $e_{tr} = 9 \times 10^{14} \text{ g/cm}^3$, $\rho_{tr} \approx 3\rho_{sat}$

In Fig. 5, we emphasise that different observational measurements become relevant to constrain different regions under the witch-hat curves, and that different combinations of observational measurements come into play at different regimes of e_{tr} . Firstly, we show that, for all three values of e_{tr} , the maximum values of Δe are constrained by the current observational inferences (see more discussion in Sec. III C). In particular, GW170817, PSR J0437-4715 and PSR J0614-3329 assist in constraining the respective maximum Δe at small, intermediate and large values of e_{tr} . Since larger values of Δe result in more compact third branches (smaller radii), the maximum Δe is bound to be constrained by the observational measurements at some point, as all of them have a minimum value in the uncertainty of the radii. However, it is subject to the fact that we did not find an EoS using our formalism that forms a second branch satisfying all the constraints by itself and then forms a third branch in the regime of the unbound region (green) discussed in Fig. 2. In such a case, finding a maximum limit on Δe using observational constraints would not be possible. The maximum values of Δe ($\Delta\rho$) were noted to be $1.59 \times 10^{15} \text{ g/cm}^3$ ($4.71\rho_{sat}$), $1.77 \times 10^{15} \text{ g/cm}^3$ ($4.98\rho_{sat}$) and $2.94 \times 10^{15} \text{ g/cm}^3$ ($7.76\rho_{sat}$) at small, intermediate and large e_{tr} , respectively.

Secondly, in Fig. 4, we observe that, even though the larger e_{tr} results in larger witch-hat curves, however, observational measurements tend to constrain these regions more tightly. We find that the collection of allowed (satisfying causality) hadronic EoSs at larger e_{tr} is softer, resulting in lower M_{TOV} . As a result, at extremely large values of e_{tr} , the hybrid EoSs consisting of such hadronic parts won't be stiff enough to satisfy the mass constraint from PSR J0348+0432. Hence, there exists a maximum value of e_{tr} for the TS solution in the light of current observational constraints (see more discussion in Sec. III C).

For small value of e_{tr} , the region under the witch-hat curve is already divided into regions of lower $(P_{tr}, \Delta e)$ and higher $(P_{tr}, \Delta e)$, as observed in Fig. 4. The three selected EoSs indicate that the allowed of M - R sequences

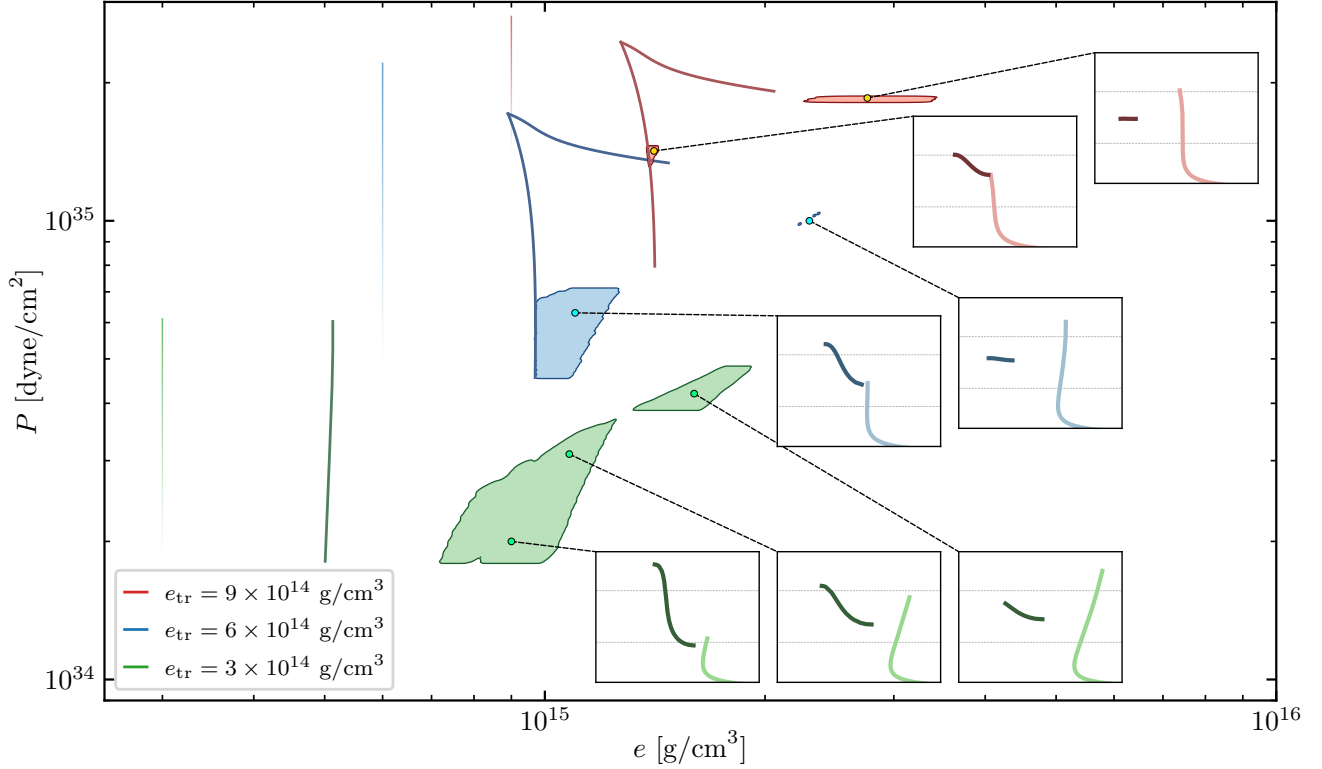


FIG. 4. Allowed regions under the witch-hat curve for three different values of e_{tr} , constrained from observational measurements (2σ confidence). The vertical fading lines indicate the value of e_{tr} . For all the EoSs, the quark part is described with $c_{s,QM}^2 = 1.0$. The inset shows the M - R sequences of the EoSs with $(P_{tr}, \Delta e)$ marked by circles inside the allowed region. Only the stable branches of M - R sequences are shown, where the second (third) branch is indicated using light (dark) colour in the respective colour theme used for the e_{tr} . Black dashed lines are marked at $1.0 M_{\odot}$ and $2.0 M_{\odot}$ for the identification of TS categories.

can span categories II, III, and IV. However, the range of EoSs that can form category II TSs appears disconnected from the range of EoSs that can form the rest of the categories. In Fig. 5, we show that the NICER measurement of PSR J0740+6620 and GW170817 are responsible (from the bottom and top, respectively) for this bifurcation. Importantly, the region of EoSs right below the tip of the witch-hat curve, which majorly constructs category I TSs, is ruled out at small e_{tr} due to the violation of constraints from PSR J0614–3329 and GW170817. These constraints demand softer hadronic parts in the EoSs, such that the second branch satisfies them and the third branch can construct massive TSs of category I.

For intermediate value of e_{tr} , we observe that the region of higher $(P_{tr}, \Delta e)$ is tightly constrained, which is linked with the category II TSs. In Fig. 5, we show that the mass-radius region inferred from GW170817 is mainly responsible for ruling out these EoSs. In particular, the second branches of these EoSs are too stiff (violating GW170817), followed by most of the third branches only satisfying the constraint of either of the companion masses in the GW170817 event. Instead, EoS with TSs of category III and IV are preferred in such a regime of e_{tr} , having the third branch covering a larger mass range

and satisfying the mass-radius constraints from both the companions of GW170817. The category I TSs are still ruled out in this regime of e_{tr} for the same reasons discussed for small e_{tr} .

For large value of e_{tr} , the regions of allowed EoSs shrink drastically, mainly violating constraints from PSR J0614–3329 and PSR J0348+0432. The set of allowed hadronic EoSs is rather soft, and only a few hybrid EoSs can produce massive NSs ($\gtrsim 2M_{\odot}$). Even though a larger range of Δe is allowed in the region of higher $(P_{tr}, \Delta e)$, the range of allowed P_{tr} for such category II TSs is tightly constrained. Therefore, the range of allowed hadronic EoSs is heavily constrained at such a regime of e_{tr} . Interestingly, EoSs with TSs of category IV are also unable to support massive NS and hence are strictly ruled out in this case. The TSs of category I still remain ruled out, as in previous cases; however, we observe that such TSs are allowed at extremely large e_{tr} (see more discussion in Sec. III C).

Since the witch-hat curves are dictated by $c_{s,QM}^2$ (as discussed in Sec. III A), the allowed regions from observations will also be affected in a similar manner. In Fig. 6, we summarise the effect of $c_{s,QM}^2$ in the picture. Since the resulting witch-hat curves are smaller with a decrease in $c_{s,QM}^2$, the observationally constrained regions are also

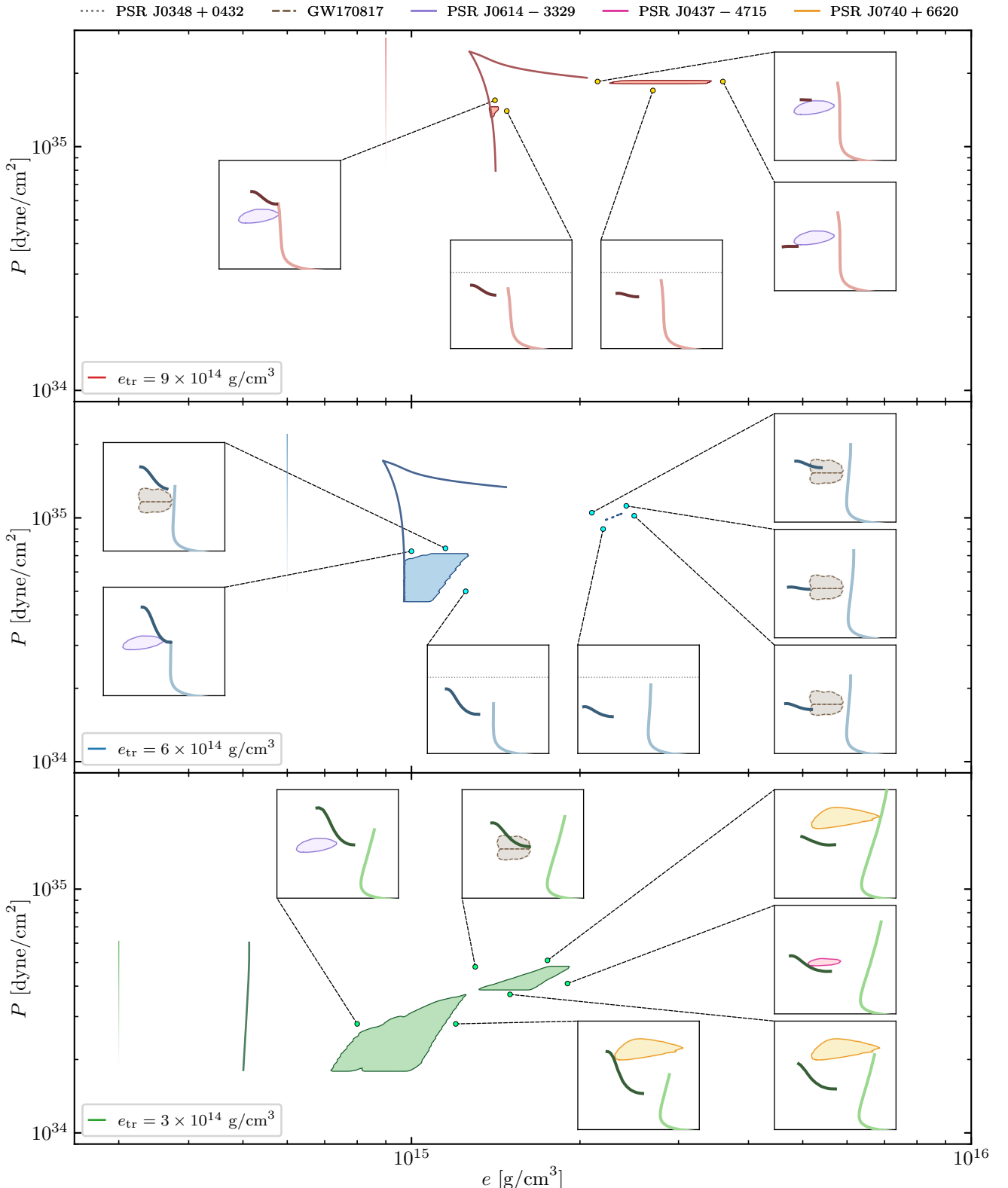


FIG. 5. Emphasis on particular observational measurements (2σ confidence) that are responsible for constraining various regions under the witch-hat curve for three different values of e_{tr} . The vertical fading lines indicate the value of e_{tr} . The quark EoS description is set with $c_{s, \text{QM}}^2 = 1.0$. The inset shows the M - R sequences, along with the particular observational constraint that they violate. These M - R sequences are constructed with the EoSs with $(P_{tr}, \Delta e)$ marked by circles outside the allowed region. Only the stable branches of M - R sequences are shown, where the second (third) branch is indicated using light (dark) colour in the respective colour theme used for the e_{tr} .

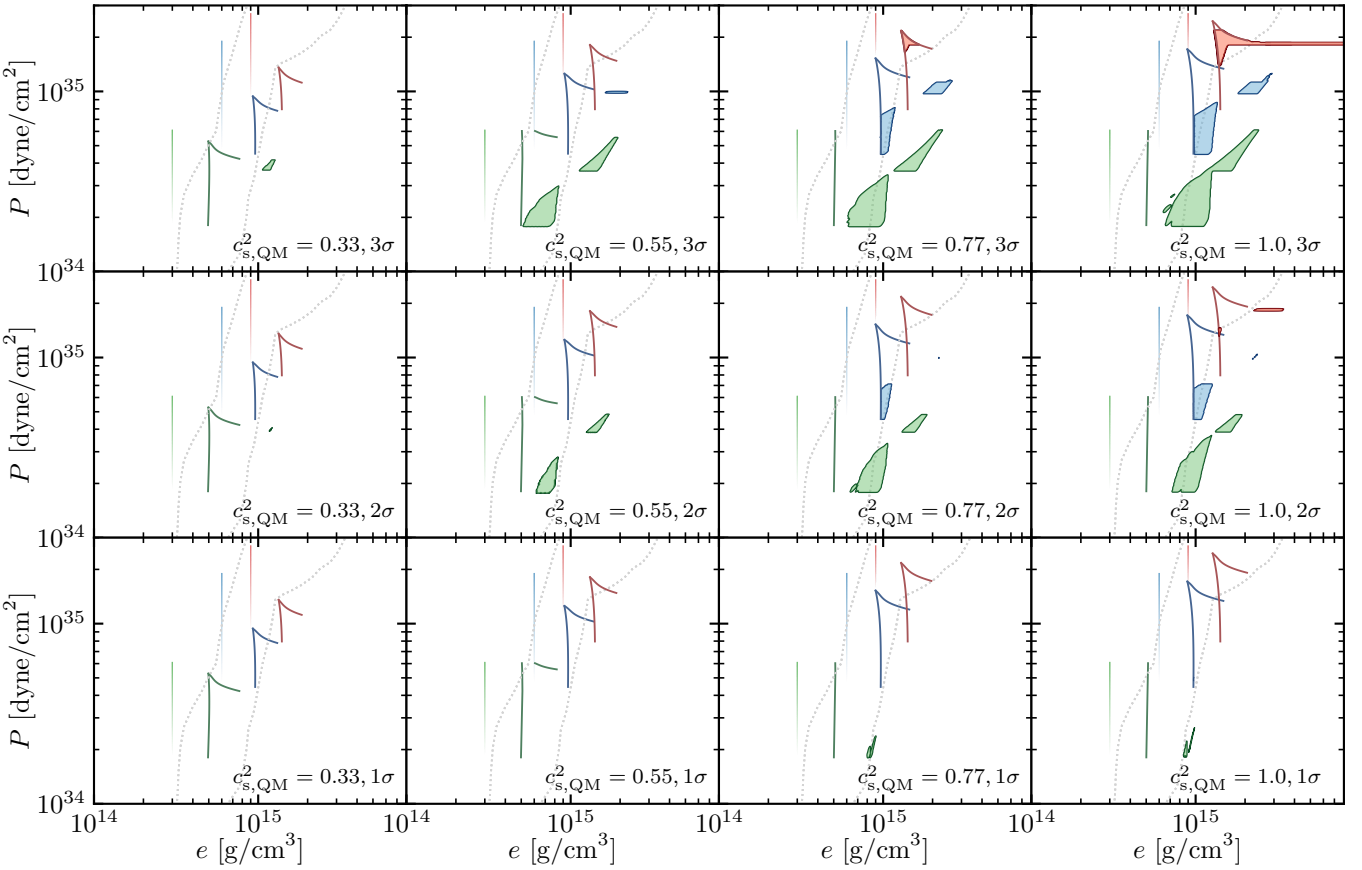


FIG. 6. Change in the picture of allowed regions of Δe with varying $c_{s,QM}^2$ (0.33, 0.55, 0.77 and 1.0) along with imposition of the constraints from observational measurements at different confidences (1 σ , 2 σ and 3 σ). The choice of $c_{s,QM}^2$ remains the same over a column, and the choice of confidence remains constant over a row. The background contour is taken from [70], indicating that the range of allowed EoSs in this study lies over (however, not completely within) the constrained region provided in the literature. The vertical fading lines indicate the value of e_{tr} .

tighter (from right to left panel). Additionally, we inform the further inclusions (rejections) of EoSs when 3 σ (1 σ) confidence of observational inferences are considered. As expected, an increase in the confidence interval (from the lower to the upper panel) widens the set of allowed EoSs. Interestingly, if 3 σ confidence is used to constrain EoSs with higher values of $c_{s,QM}^2$ (0.77 and 1.0), we observe that the EoSs with category I TSs are included at large values of e_{tr} , which remained excluded in our examination while considering 2 σ confidence of observational data. Secondly, at large e_{tr} with $c_{s,QM}^2 = 1.0$, we observe that a slim range of P_{tr} is allowed with Δe being unconstrained. These hybrid EoSs construct a second branch that satisfies all the constraints while having its P_{tr} in the unbound region (green), as discussed in Fig. 2. However, in the interest of extending these hybrid EoSs to match the known behaviour of matter at pQCD regime (see Refs. [70, 73, 93] for such consistency treatments to agnostic EoSs), an ultimate upper bound can be drawn on Δe ($\Delta\rho$) to be $\sim 5 \times 10^{15}$ g/cm³ ($\sim 13\rho_{sat}$).

For 1 σ confidence level, hybrid EoSs are only allowed with a stiffer quark part. Additionally, the allowed EoSs

specifically have lower values of P_{tr} , indicating that only category III and IV TSs can comply with such constraints, and thereby strictly excluding category I and category II TSs. On a side note, we did not find the PSR J0030+0451 inference useful for constraining any part of this picture.

C. Limits on properties of PT and maximum mass of TSs

In Table I, we note the EoSs with the maximum value of e_{tr} (e_{tr}^{\max}), for varying stiffness of quark EoS. Interestingly, the EoSs that form category I TSs are allowed at extremely large e_{tr} ($\approx 4\rho_{sat}$), and are consequently responsible for setting the upper bound on e_{tr} . Such hybrid EoSs are soft enough to construct second branches that follow all the constraints (2 σ confidence level) while supporting massive TSs on the third branch. Since P_{tr} of these EoSs lie in the bound region (blue) of the witch-hat curve, the maximum of Δe is strictly decided from TOV solutions. In the cases of softer quark EoSs, the

TABLE I. Maximum transition energy density (e_{tr}^{\max}) and respective maximum transition rest-mass density (ρ_{tr}^{\max}) for various stiffnesses of quark matter EoSs using $c_{s,\text{QM}}^2$. The values of Δe and $\Delta \rho$ are also noted for these selected EoSs, along with their category of TSs. This computation is performed considering 2σ confidence level.

$c_{s,\text{QM}}^2$	e_{tr}^{\max} [g/cm ³]	Δe [g/cm ³]	ρ_{tr}^{\max} [ρ_{sat}]	$\Delta \rho$ [ρ_{sat}]	Category
1.0	1.40×10^{15}	0.48×10^{15}	4.03	1.14	I
0.85	1.27×10^{15}	0.46×10^{15}	3.70	1.14	I
0.55	0.54×10^{15}	0.33×10^{15}	1.87	1.04	III
0.33	0.33×10^{15}	0.91×10^{15}	1.18	2.75	II

TABLE II. Maximum transition energy density (e_{tr}^{\max}) and respective maximum transition rest-mass density (ρ_{tr}^{\max}) under different confidence levels of constraints from observational inferences. The values of Δe and $\Delta \rho$ are also noted for these selected EoSs, along with their category of TSs. This computation is performed considering the stiffest quark EoS ($c_{s,\text{QM}}^2 = 1.0$).

Confidence	e_{tr}^{\max} [g/cm ³]	Δe [g/cm ³]	ρ_{tr}^{\max} [ρ_{sat}]	$\Delta \rho$ [ρ_{sat}]	Category
3σ	1.40×10^{15}	0.48×10^{15}	4.03	1.14	I
2σ	1.40×10^{15}	0.48×10^{15}	4.03	1.14	I
1σ	0.42×10^{15}	0.49×10^{15}	1.48	1.61	III

TABLE III. Maximum strength of PT discontinuity in energy density (Δe_{\max}) and respective rest-mass density ($\Delta \rho_{\max}$) for various stiffnesses of quark matter EoSs using $c_{s,\text{QM}}^2$. The values of e_{tr} and ρ_{tr} are also noted for the allowed EoS along with their category of TSs. This computation is performed considering 2σ confidence level.

$c_{s,\text{QM}}^2$	Δe_{\max} [g/cm ³]	$\Delta \rho_{\max}$ [ρ_{sat}]	e_{tr} [g/cm ³]	ρ_{tr} [ρ_{sat}]	Category
1.0	2.94×10^{15}	7.76	0.90×10^{15}	2.92	II
0.85	2.35×10^{15}	6.29	0.88×10^{15}	2.85	II
0.55	1.43×10^{15}	4.10	0.49×10^{15}	1.67	II
0.33	0.92×10^{15}	2.80	0.32×10^{15}	1.12	II

TABLE IV. Maximum strength of PT discontinuity in energy density (Δe_{\max}) and respective rest-mass density ($\Delta \rho_{\max}$) under different confidence levels of constraints from observational inferences. The values of e_{tr} and ρ_{tr} are also noted for the allowed EoS along with their category of TSs. This computation is done for the stiffest quark EoS ($c_{s,\text{QM}}^2 = 1.0$).

Confidence	Δe_{\max} [g/cm ³]	$\Delta \rho_{\max}$ [ρ_{sat}]	e_{tr} [g/cm ³]	ρ_{tr} [ρ_{sat}]	Category
3σ	4.97×10^{15}	13.13	0.90×10^{15}	2.92	II
2σ	2.94×10^{15}	7.76	0.90×10^{15}	2.92	II
1σ	0.68×10^{15}	2.21	0.30×10^{15}	1.06	III

TABLE V. Maximum mass of TSs (M_{TS}^{\max}) and their categories, for various stiffnesses of quark matter EoSs using $c_{s,\text{QM}}^2$. The values of Δe and $\Delta \rho$ are also noted for the allowed EoS that construct the stellar configurations supporting M_{TS}^{\max} . This computation is performed considering 2σ confidence level.

$c_{s,\text{QM}}^2$	M_{TS}^{\max} [M_{\odot}]	e_{tr} [g/cm ³]	Δe [g/cm ³]	ρ_{tr} [ρ_{sat}]	$\Delta \rho$ [ρ_{sat}]	Category
1.0	2.05	1.26×10^{15}	0.45×10^{15}	3.66	1.10	I
0.85	2.02	1.21×10^{15}	0.45×10^{15}	3.55	1.10	I
0.55	1.57	0.30×10^{15}	1.09×10^{15}	1.03	3.22	II
0.33	1.38	0.30×10^{15}	0.67×10^{15}	1.03	2.17	II

TABLE VI. Maximum mass of TSs (M_{TS}^{\max}) and their categories, under different confidence levels of constraints from observational inferences. The values of Δe and $\Delta \rho$ are also noted for the allowed EoS that construct the stellar configurations supporting M_{TS}^{\max} . This computation is performed considering the stiffest quark EoS ($c_{s,\text{QM}}^2 = 1.0$).

Confidence	M_{TS}^{\max} [M_{\odot}]	e_{tr} [g/cm ³]	Δe [g/cm ³]	ρ_{tr} [ρ_{sat}]	$\Delta \rho$ [ρ_{sat}]	Category
3σ	2.32	0.97×10^{15}	0.39×10^{15}	2.92	0.94	I
2σ	2.05	1.26×10^{15}	0.45×10^{15}	3.66	1.01	I
1σ	1.37	0.3×10^{15}	0.67×10^{15}	1.03	2.17	III

hybrid EoSs do not support massive TSs to satisfy the mass constraint from PSR J0348+0432. It can be anticipated from Fig. 3 where we show that smaller $c_{s,\text{QM}}^2$ sets smaller P_{tr}^{\max} . It suggests that a second branch supports massive NSs ($\gtrsim 2.0 M_{\odot}$) that will have central pressures higher than P_{tr}^{\max} , and for such EoSs, TS solutions would not exist. In such cases, e_{tr}^{\max} is achieved via EoSs with TSs of categories II–III, which is the reason behind the e_{tr}^{\max} being drastically smaller than we found for stiffer quark EoSs. In Table II, we find the e_{tr}^{\max} for various confidence intervals using the stiffest quark EoS. The results remain unchanged for 2σ and 3σ confidence levels, as these results are mainly bound by mass constraint from PSR J0348+0432. For 1σ , the observational constraints demand even more compact second branch around the canonical NS mass ($1.4 M_{\odot}$). A hybrid EoS with such a soft hadronic part fails to support massive TSs of category I. In compliance with 1σ confidence level, e_{tr}^{\max} is established at a much smaller value by an EoS with TSs of category III.

Similarly, in Tables III and IV, we note the EoSs with the maximum value of Δe (Δe_{\max}). These inferences are made out of EoSs that construct TSs of category II (except for the case of 1σ confidence interval that only allows TSs of category III and IV). For a stiffer quark EoS, the hybrid EoSs construct a second branch that satisfies all observations except for PSR J0614–3329. The third branch of category II kind then satisfies PSR J0614–3329, resulting in inclusion of such an EoS with large Δe . For a softer quark EoS, the hybrid EoSs construct a second branch that satisfies the observation PSR J0740+6630, whereas the third branch of category II kind then satisfies the rest of the constraints. For 1σ confidence level, an EoS with TSs of category III decides the Δe_{\max} , where the third branch satisfies all the constraints.

In Table V, we noted the maximum mass of the TSs (M_{TS}^{\max}) considering various stiffnesses of quark matter EoS (not to be confused with $M_{\text{TOV},3}$ as defined in Sec. II A). For soft quark EoSs, we observe that the M_{TS}^{\max} is achieved for $\rho_{\text{tr}} \sim 1\rho_{\text{sat}}$, which is at the limit of our analysis. Higher M_{TS}^{\max} can be found for lower ρ_{tr} , but it will be very low for a hadron-to-quark PT. In Table VI, we noted the M_{TS}^{\max} considering various confidence intervals of observational constraints. For 2σ and 3σ confidence, we observe that $M_{\text{TS}}^{\max} > 2.0 M_{\odot}$, constructed out of category I TSs. For 1σ confidence level infers $M_{\text{TS}}^{\max} = 1.37 M_{\odot}$, which is drastically smaller, and is a manifestation of allowing only category III and IV TSs.

IV. CONCLUSIONS

We performed a thorough analysis of hybrid EoSs with strong first-order (Maxwell-type) PT, which can form TS solutions. We employ an agnostic approach for the systematic construction of EoSs mainly using the four parameters—transition energy density (e_{tr}) and transition pressure (P_{tr}), the strength of discontinuity in

energy density (Δe) and constant speed of sound for quark matter EoS ($c_{s,\text{QM}}^2$).

Given the setup of our parameter space, we systematically present a comprehensive picture of the conditions required by the hybrid EoSs to form TSs. These conditions are purely achieved from TOV solutions within the causality limit. For a fixed value of e_{tr} and $c_{s,\text{QM}}^2$, we define three regions of P_{tr} :

- *solution-less region*—TSs do not form for any Δe
- *bound region*—TSs form for a range of Δe
- *unbound region*—TSs form beyond a minimum limit on Δe

In this article, the loci of minimum and maximum Δe are tossed as the ‘witch-hat’ curves. We show that a witch-hat curve can be described for a given $(e_{\text{tr}}, c_{s,\text{QM}}^2)$, where each point $(P_{\text{tr}}, \Delta e)$ under this curve represents a hybrid EoS that can form TSs. We find that an increase in the values of e_{tr} or $c_{s,\text{QM}}^2$ enlarges its witch-hat curve, thereby allowing a larger range of EoSs to form TSs. For certain combinations of $(e_{\text{tr}}, c_{s,\text{QM}}^2)$, witch-hat curves can be punctured (or incomplete) based on the causality limit. We observed that the TOV solutions can put only an upper limit on P_{tr} (if not by the causality limit). No upper limit is provided for the e_{tr} or Δe (at small values of P_{tr}). However, the recent observational measurements provide strong constraints on this picture.

We explain the constrained picture from the observational inferences (2σ confidence level) on the region under the witch-hat curves for three values of e_{tr} (qualitatively at small, intermediate and large values) with fixed $c_{s,\text{QM}}^2 = 1.0$ (stiffest quark EoS). We find that different observational measurements are relevant for constraining different regions under the witch-hat curves, and that different combinations of measurements come into play at different regimes of e_{tr} . The constraints split the allowed region under the witch-hat curve into two fractions—(i) region of lower $(P_{\text{tr}}, \Delta e)$, forming TSs of category III and IV, and (ii) region of higher $(P_{\text{tr}}, \Delta e)$, forming TSs of category II. We observe that TSs of category I are only allowed at extremely large values of e_{tr} ($\approx 4\rho_{\text{sat}}$). As the e_{tr} increases, the observational inferences constrain the regions under the witch-hat curves more tightly.

Importantly, a maximum limit on Δe is sufficiently provided for all values of e_{tr} . We note that a maximum limit on e_{tr} is also provided, as an increase in e_{tr} allows softer hadronic EoSs which are tightly constrained when such hybrid EoSs are unable to support massive NSs ($\gtrsim 2.0 M_{\odot}$). On the other hand, we found a maximum mass for the TSs. While keeping the stiffest quark EoS ($c_{s,\text{QM}}^2 = 1.0$), we report the following thermodynamic and astrophysical upper bounds:

- $e_{\text{tr}}^{\max} = 1.4 \times 10^{15} \text{ g/cm}^3$ ($\rho_{\text{tr}}^{\max} = 4.03\rho_{\text{sat}}$), governed by an EoS with TSs of category I
- $\Delta e_{\max} = 2.94 \times 10^{15} \text{ g/cm}^3$ ($\Delta\rho_{\max} = 7.75\rho_{\text{sat}}$), governed by an EoS with TSs of category II

- $M_{\text{TS}}^{\text{max}} = 2.05 M_{\odot}$, governed by an EoS with TSs of category I

Naturally, for a softer quark EoS, these limits will be affected, the results of which are summarised in the dedicated tables. We note that the contributing categories of TSs change when softer quark EoSs are considered.

These bounds and inferences are further affected by considering different confidence levels for the observational inferences. In particular, confidence levels of 1σ change the inferences drastically. In such tight constraints, the bounds— $e_{\text{tr}}^{\text{max}}$, Δe_{max} and $M_{\text{TS}}^{\text{max}}$ are instead provided by the EoSs that can form TSs of category II and III, as category I TSs are completely ruled out. On the other side, we note that confidence levels of 3σ fail to place an upper bound on Δe at large values of e_{tr} . Under such relaxed constraints, the allowed EoSs (although for a small range of P_{tr}) can have a second branch on the M – R sequence that satisfies all the observations, while having its P_{tr} in the unbound region. Such cases were not found at 1σ and 2σ confidence levels, placing strict upper bounds on Δe .

Observation of TSs (especially massive ones like the $M_{\text{TS}}^{\text{max}}$), can be smoking gun signatures of PT in the density regimes present in the cores of NSs. As found in this study, these can immediately place strong constraints on the e_{tr} and Δe , and significantly further our understanding of the possible nature of hadron-to-quark PT that can exist at such high densities. It would be interesting to consider additional effects, such as rotation and magnetic field, to gain a complete insight into this picture. A com-

plementary study should also be drawn by considering a different class of PT with a non-vanishing speed of sound (for instance, the impact of varying surface tension at the interface of phases [138–143]). A parallel study has implemented speed of sound parametrisation to define the hadronic and quark EoSs for the class of EoSs that construct TS [93], in contrast to the implementation of a piecewise polytrope with the CSS formalism used in this study.

ACKNOWLEDGEMENTS

It is a pleasure to thank Sagnik Chatterjee for his crucial insights into this work. The authors also express their gratitude to the Deucalion HPC in Portugal for its support in the Advanced Computing Project 2025.00067.CPCA A3, RNCA (Rede Nacional de Computação Avançada), financed by the FCT (Fundação para a Ciência e a Tecnologia, IP, Portugal). The test setups were completed in the National Supercomputing Mission (NSM) resource ‘PARAM Ganga’ at IIT Roorkee, which is implemented by C-DAC and supported by the Ministry of Electronics and Information Technology (MeitY) and the Department of Science and Technology (DST), Government of India. The small-scale tests were conducted at the Bhaskara HPC in IISER Bhopal. SH and RM acknowledge the SERB grant: CRG/2022/000663. This research work is done using the packages—NUMPY [144], SCIPTY [145], MATPLOTLIB [146], SEABORN [147], JUPYTER [148], NUMBA [149] and OPENCV [150].

[1] R. Kumar *et al.*, Theoretical and experimental constraints for the equation of state of dense and hot matter, *Living Rev Relativ* **27**, 3 (2024).

[2] J. M. Lattimer, Neutron Stars and the Nuclear Matter Equation of State, *Annual Review of Nuclear and Particle Science* **71**, 433 (2021).

[3] K. Chatzioannou *et al.*, Neutron stars and the dense matter equation of state, *Rev. Mod. Phys.* **97**, 045007 (2025).

[4] N. K. Glendenning, *Compact Stars* (Springer, 1997).

[5] J. M. Lattimer and M. Prakash, The Physics of Neutron Stars, *Science* **304**, 536 (2004).

[6] A. Annala, Neutron star characteristics from the neutron structure, *Front. Phys.* **11**, 1286802 (2023).

[7] G. F. Burgio, H. J. Schulze, I. Vidaña, and J. B. Wei, Neutron stars and the nuclear equation of state, *Progress in Particle and Nuclear Physics* **120**, 103879 (2021).

[8] G. Baym, T. Hatsuda, T. Kojo, P. D. Powell, Y. Song, and T. Takatsuka, From hadrons to quarks in neutron stars: A review, *Rep. Prog. Phys.* **81**, 056902 (2018).

[9] E. V. Shuryak, Quantum chromodynamics and the theory of superdense matter, *Physics Reports* **61**, 71 (1980).

[10] J. Keller, K. Hebeler, and A. Schwenk, Nuclear Equation of State for Arbitrary Proton Fraction and Temperature Based on Chiral Effective Field Theory and a Gaussian Process Emulator, *Phys. Rev. Lett.* **130**, 072701 (2023).

[11] I. Tews, J. Carlson, S. Gandolfi, and S. Reddy, Constraining the Speed of Sound inside Neutron Stars with Chiral Effective Field Theory Interactions and Observations, *ApJ* **860**, 149 (2018).

[12] C. Drischler, R. J. Furnstahl, J. A. Melendez, and D. R. Phillips, How Well Do We Know the Neutron-Matter Equation of State at the Densities Inside Neutron Stars? A Bayesian Approach with Correlated Uncertainties, *Phys. Rev. Lett.* **125**, 202702 (2020).

[13] C. Drischler, K. Hebeler, and A. Schwenk, Chiral Interactions up to Next-to-Next-to-Next-to-Leading Order and Nuclear Saturation, *Phys. Rev. Lett.* **122**, 042501 (2019).

[14] K. Hebeler, J. M. Lattimer, C. J. Pethick, and A. Schwenk, Equation of State and Neutron Star Properties Constrained by Nuclear Physics and Observation, *ApJ* **773**, 11 (2013).

[15] M. G. Alford, L. Brodie, A. Haber, and I. Tews, Relativistic mean-field theories for neutron-star physics

based on chiral effective field theory, *Phys. Rev. C* **106**, 055804 (2022).

[16] C. Drischler, J. W. Holt, and C. Wellenhofer, Chiral Effective Field Theory and the High-Density Nuclear Equation of State, *Annual Review of Nuclear and Particle Science* **71**, 403 (2021).

[17] D. Lonardoni, I. Tews, S. Gandolfi, and J. Carlson, Nuclear and neutron-star matter from local chiral interactions, *Phys. Rev. Research* **2**, 022033 (2020).

[18] J. W. Holt and N. Kaiser, Equation of state of nuclear and neutron matter at third-order in perturbation theory from chiral effective field theory, *Phys. Rev. C* **95**, 034326 (2017).

[19] K. Hebeler, J. D. Holt, J. Menéndez, and A. Schwenk, Nuclear Forces and Their Impact on Neutron-Rich Nuclei and Neutron-Rich Matter, *Annual Review of Nuclear and Particle Science* **65**, 457 (2015).

[20] C. Drischler, V. Somà, and A. Schwenk, Microscopic calculations and energy expansions for neutron-rich matter, *Phys. Rev. C* **89**, 025806 (2014).

[21] R. Machleidt and D. R. Entem, Chiral effective field theory and nuclear forces, *Physics Reports* **503**, 1 (2011).

[22] E. Epelbaum, H.-W. Hammer, and U.-G. Meißner, Modern theory of nuclear forces, *Rev. Mod. Phys.* **81**, 1773 (2009).

[23] J. Adams *et al.*, Experimental and theoretical challenges in the search for the quark-gluon plasma: The STAR Collaboration's critical assessment of the evidence from RHIC collisions, *Nuclear Physics A* **757**, 102 (2005).

[24] I. Arsene *et al.*, Quark-gluon plasma and color glass condensate at RHIC? The perspective from the BRAHMS experiment, *Nuclear Physics A First Three Years of Operation of RHIC*, **757**, 1 (2005).

[25] B. B. Back *et al.*, The PHOBOS perspective on discoveries at RHIC, *Nuclear Physics A First Three Years of Operation of RHIC*, **757**, 28 (2005).

[26] K. Adcox *et al.*, Formation of dense partonic matter in relativistic nucleus-nucleus collisions at RHIC: Experimental evaluation by the PHENIX Collaboration, *Nuclear Physics A First Three Years of Operation of RHIC*, **757**, 184 (2005).

[27] T. Gehrman and B. Malaescu, Precision QCD Physics at the LHC, *Annual Review of Nuclear and Particle Science* **72**, 233 (2022).

[28] A. Bazavov *et al.*, Equation of state and QCD transition at finite temperature, *Phys. Rev. D* **80**, 014504 (2009).

[29] S. Borsányi, Z. Fodor, C. Hoelbling, S. D. Katz, S. Krieg, and K. K. Szabó, Full result for the QCD equation of state with 2 + 1 flavors, *Physics Letters B* **730**, 99 (2014).

[30] K. Nagata, Finite-density lattice QCD and sign problem: Current status and open problems, *Progress in Particle and Nuclear Physics* **127**, 103991 (2022).

[31] M. Troyer and U.-J. Wiese, Computational Complexity and Fundamental Limitations to Fermionic Quantum Monte Carlo Simulations, *Phys. Rev. Lett.* **94**, 170201 (2005).

[32] V. A. Goy, V. Bornyakov, D. Boyd, A. Molochkov, A. Nakamura, A. Nikolaev, and V. Zakharov, Sign problem in finite density lattice QCD, *Progress of Theoretical and Experimental Physics* **2017**, 10.1093/ptep/ptx018 (2017).

[33] J. O. Andersen, M. Strickland, and N. Su, Gluon Thermodynamics at Intermediate Coupling, *Phys. Rev. Lett.* **104**, 122003 (2010).

[34] J. O. Andersen, L. E. Leganger, M. Strickland, and N. Su, QCD trace anomaly, *Phys. Rev. D* **84**, 087703 (2011).

[35] T. Gorda and S. Säppi, Cool quark matter with perturbative quark masses, *Phys. Rev. D* **105**, 114005 (2022).

[36] S. Mogliacci, J. O. Andersen, M. Strickland, N. Su, and A. Vuorinen, Equation of state of hot and dense QCD: Resummed perturbation theory confronts lattice data, *J. High Energ. Phys.* **2013** (12), 55.

[37] T. Gorda, R. Paatelainen, S. Säppi, and K. Seppänen, Equation of State of Cold Quark Matter to O ($\alpha s \ln \alpha s$), *Phys. Rev. Lett.* **131**, 181902 (2023).

[38] T. Gorda, A. Kurkela, R. Paatelainen, S. Säppi, and A. Vuorinen, Soft Interactions in Cold Quark Matter, *Phys. Rev. Lett.* **127**, 162003 (2021).

[39] T. Gorda, A. Kurkela, P. Romatschke, M. Säppi, and A. Vuorinen, Next-to-Next-to-Next-to-Leading Order Pressure of Cold Quark Matter: Leading Logarithm, *Phys. Rev. Lett.* **121**, 202701 (2018).

[40] A. Kurkela and A. Vuorinen, Cool Quark Matter, *Phys. Rev. Lett.* **117**, 042501 (2016).

[41] A. Kurkela, P. Romatschke, and A. Vuorinen, Cold quark matter, *Phys. Rev. D* **81**, 105021 (2010).

[42] N. Haque, A. Bandyopadhyay, J. O. Andersen, M. G. Mustafa, M. Strickland, and N. Su, Three-loop HTLpt thermodynamics at finite temperature and chemical potential, *J. High Energ. Phys.* **2014** (5), 27.

[43] N. Haque and M. Strickland, Next-to-next-to leading-order hard-thermal-loop perturbation-theory predictions for the curvature of the QCD phase transition line, *Phys. Rev. C* **103**, L031901 (2021).

[44] J. Ghiglieri, A. Kurkela, M. Strickland, and A. Vuorinen, Perturbative thermal QCD: Formalism and applications, *Physics Reports* **880**, 1 (2020).

[45] T. E. Riley *et al.*, A NICER View of PSR J0030+0451: Millisecond Pulsar Parameter Estimation, *ApJL* **887**, L21 (2019).

[46] M. C. Miller *et al.*, PSR J0030+0451 Mass and Radius from NICER Data and Implications for the Properties of Neutron Star Matter, *ApJL* **887**, L24 (2019).

[47] G. Raaijmakers *et al.*, A NICER View of PSR J0030+0451: Implications for the Dense Matter Equation of State, *ApJL* **887**, L22 (2019).

[48] T. E. Riley *et al.*, A NICER View of the Massive Pulsar PSR J0740+6620 Informed by Radio Timing and XMM-Newton Spectroscopy, *ApJL* **918**, L27 (2021).

[49] M. C. Miller *et al.*, The Radius of PSR J0740+6620 from NICER and XMM-Newton Data, *ApJL* **918**, L28 (2021).

[50] G. Raaijmakers *et al.*, Constraints on the Dense Matter Equation of State and Neutron Star Properties from NICER's Mass-Radius Estimate of PSR J0740+6620 and Multimessenger Observations, *ApJL* **918**, L29 (2021).

[51] E. Fonseca *et al.*, Refined Mass and Geometric Measurements of the High-mass PSR J0740+6620, *ApJL* **915**, L12 (2021).

[52] L. Mauviard *et al.*, A NICER View of the 1.4 M \odot Edge-on Pulsar PSR J0614-3329, *ApJ* **995**, 60 (2025).

[53] D. Choudhury *et al.*, A NICER View of the Nearest and Brightest Millisecond Pulsar: PSR J0437-4715, *ApJL* **971**, L20 (2024).

[54] B. P. Abbott *et al.*, GW170817: Observation of Gravitational Waves from a Binary Neutron Star Inspiral, *Phys. Rev. Lett.* **119**, 161101 (2017).

[55] C. A. Raithel, F. Özel, and D. Psaltis, Tidal Deformability from GW170817 as a Direct Probe of the Neutron Star Radius, *ApJL* **857**, L23 (2018).

[56] S. De, D. Finstad, J. M. Lattimer, D. A. Brown, E. Berger, and C. M. Biwer, Tidal Deformabilities and Radii of Neutron Stars from the Observation of GW170817, *Phys. Rev. Lett.* **121**, 091102 (2018).

[57] L. Rezzolla, E. R. Most, and L. R. Weih, Using Gravitational-wave Observations and Quasi-universal Relations to Constrain the Maximum Mass of Neutron Stars, *ApJL* **852**, L25 (2018).

[58] A. Bauswein, O. Just, H.-T. Janka, and N. Stergioulas, Neutron-star Radius Constraints from GW170817 and Future Detections, *ApJL* **850**, L34 (2017).

[59] E. Annala, T. Gorda, A. Kurkela, and A. Vuorinen, Gravitational-Wave Constraints on the Neutron-Star-Matter Equation of State, *Phys. Rev. Lett.* **120**, 172703 (2018).

[60] B. P. Abbott *et al.*, GW170817: Measurements of Neutron Star Radii and Equation of State, *Phys. Rev. Lett.* **121**, 161101 (2018).

[61] F. Özel, D. Psaltis, S. Ransom, P. Demorest, and M. Alford, The Massive Pulsar PSR J1614-2230: Linking Quantum Chromodynamics, Gamma-ray Bursts, and Gravitational Wave Astronomy, *ApJL* **724**, L199 (2010).

[62] H. T. Cromartie *et al.*, Relativistic Shapiro delay measurements of an extremely massive millisecond pulsar, *Nat Astron* **4**, 72 (2020).

[63] J. Antoniadis *et al.*, A Massive Pulsar in a Compact Relativistic Binary, *Science* **340**, 1233232 (2013).

[64] Z. Arzoumanian *et al.*, The NANOGrav 11-year Data Set: High-precision Timing of 45 Millisecond Pulsars, *ApJS* **235**, 37 (2018).

[65] P. B. Demorest, T. Pennucci, S. M. Ransom, M. S. E. Roberts, and J. W. T. Hessels, A two-solar-mass neutron star measured using Shapiro delay, *Nature* **467**, 1081 (2010).

[66] T. Gorda, K. Hebeler, A. Kurkela, A. Schwenk, and A. Vuorinen, Constraints on Strong Phase Transitions in Neutron Stars, *ApJ* **955**, 100 (2023).

[67] T. Gorda, O. Komoltsev, and A. Kurkela, Ab-initio QCD Calculations Impact the Inference of the Neutron-star-matter Equation of State, *ApJ* **950**, 107 (2023).

[68] R. Somasundaram, I. Tews, and J. Margueron, Investigating signatures of phase transitions in neutron-star cores, *Phys. Rev. C* **107**, 025801 (2023).

[69] L. Lindblom and N. M. Indik, Spectral approach to the relativistic inverse stellar structure problem, *Phys. Rev. D* **86**, 084003 (2012).

[70] E. Annala, T. Gorda, A. Kurkela, J. Nättilä, and A. Vuorinen, Evidence for quark-matter cores in massive neutron stars, *Nat. Phys.* **16**, 907 (2020).

[71] N. K. Glendenning, Phase transitions and crystalline structures in neutron star cores, *Physics Reports* **342**, 393 (2001).

[72] N. K. Glendenning, First-order phase transitions with more than one conserved charge: Consequences for neutron stars, *Phys. Rev. D* **46**, 1274 (1992).

[73] S. Altiparmak, C. Ecker, and L. Rezzolla, On the Sound Speed in Neutron Stars, *ApJL* **939**, L34 (2022).

[74] J. S. Read, B. D. Lackey, B. J. Owen, and J. L. Friedman, Constraints on a phenomenologically parametrized neutron-star equation of state, *Phys. Rev. D* **79**, 124032 (2009).

[75] M. F. O’Boyle, C. Markakis, N. Stergioulas, and J. S. Read, Parametrized equation of state for neutron star matter with continuous sound speed, *Phys. Rev. D* **102**, 083027 (2020).

[76] S. Chatterjee, H. Sudhakaran, and R. Mallick, Analyzing the speed of sound in neutron star with machine learning, *Eur. Phys. J. C* **84**, 1291 (2024).

[77] R. C. Tolman, Static Solutions of Einstein’s Field Equations for Spheres of Fluid, *Phys. Rev.* **55**, 364 (1939).

[78] J. R. Oppenheimer and G. M. Volkoff, On Massive Neutron Cores, *Phys. Rev.* **55**, 374 (1939).

[79] M. G. Alford, S. Han, and M. Prakash, Generic conditions for stable hybrid stars, *Phys. Rev. D* **88**, 083013 (2013).

[80] J.-E. Christian, A. Zacchi, and J. Schaffner-Bielich, Classifications of twin star solutions for a constant speed of sound parameterized equation of state, *Eur. Phys. J. A* **54**, 28 (2018).

[81] A. Zacchi, L. Tolos, and J. Schaffner-Bielich, Twin stars within the SU(3) chiral quark-meson model, *Phys. Rev. D* **95**, 103008 (2017).

[82] M. Mendes, J.-E. Christian, F. J. Fattoyev, and J. Schaffner-Bielich, Constraining twin stars with cold neutron star cooling data, *Phys. Rev. D* **111**, 063007 (2025).

[83] G. Montaña, L. Tolós, M. Hanuske, and L. Rezzolla, Constraining twin stars with GW170817, *Phys. Rev. D* **99**, 103009 (2019).

[84] L. Tsaloukidis, P. S. Koliogiannis, A. Kanakis-Pegios, and Ch. C. Moustakidis, Twin stars as probes of the nuclear equation of state: Effects of rotation through the PSR J0952-0607 pulsar and constraints via the tidal deformability from the GW170817 event, *Phys. Rev. D* **107**, 023012 (2023).

[85] J.-E. Christian and J. Schaffner-Bielich, Twin Stars and the Stiffness of the Nuclear Equation of State: Ruling Out Strong Phase Transitions below 1.7 n0 with the New NICER Radius Measurements, *ApJL* **894**, L8 (2020).

[86] J.-E. Christian and J. Schaffner-Bielich, Confirming the Existence of Twin Stars in a NICER Way, *ApJ* **935**, 122 (2022).

[87] J. J. Li, A. Sedrakian, and M. Alford, Confronting new NICER mass-radius measurements with phase transition in dense matter and twin compact stars, *J. Cosmol. Astropart. Phys.* **2025** (02), 002.

[88] P. Landry and K. Chakravarti, Prospects for constraining twin stars with next-generation gravitational-wave detectors (2022), arXiv:2212.09733 [astro-ph].

[89] D. E. Alvarez-Castillo, Properties of the Object HESS J1731-347 as a Twin Compact Star, *Universe* **11**, 224 (2025).

[90] X. Grundler and B.-A. Li, Bayesian Quantification of Observability and Equation of State of Twin Stars (2025).

[91] J. J. Li, A. Sedrakian, and M. Alford, Hybrid Star Models in the Light of New Multimessenger Data, *ApJ* **967**, 116 (2024).

[92] J.-E. Christian, J. Schaffner-Bielich, and S. Rosswog, Which first order phase transitions to quark matter are possible in neutron stars?, *Phys. Rev. D* **109**, 063035 (2024).

[93] S. Blomqvist, C. Ecker, T. Gorda, and A. Vuorinen, Strong model-agnostic constraints for twin-star solutions (2025), arXiv:2512.19477 [astro-ph].

[94] D. E. Alvarez-Castillo, D. B. Blaschke, A. G. Grunfeld, and V. P. Pagura, Third family of compact stars within a nonlocal chiral quark model equation of state, *Phys. Rev. D* **99**, 063010 (2019).

[95] S. Benić, D. Blaschke, D. E. Alvarez-Castillo, T. Fischer, and S. Typel, A new quark-hadron hybrid equation of state for astrophysics - I. High-mass twin compact stars, *A&A* **577**, A40 (2015).

[96] V. P. Gonçalves, L. Lazzari, and J. C. Jiménez, Electrically charged supermassive twin stars, *Eur. Phys. J. C* **82**, 110 (2022).

[97] J.-E. Christian and J. Schaffner-Bielich, Supermassive neutron stars rule out twin stars, *Phys. Rev. D* **103**, 063042 (2021).

[98] D. E. Alvarez-Castillo and D. B. Blaschke, High-mass twin stars with a multipolytrope equation of state, *Phys. Rev. C* **96**, 045809 (2017).

[99] P. L. Espino and V. Paschalidis, Fate of twin stars on the unstable branch: Implications for the formation of twin stars, *Phys. Rev. D* **105**, 043014 (2022).

[100] M. Naseri, G. Bozzola, and V. Paschalidis, Exploring pathways to forming twin stars, *Phys. Rev. D* **110**, 044037 (2024).

[101] M. Alford and A. Sedrakian, Compact Stars with Sequential QCD Phase Transitions, *Phys. Rev. Lett.* **119**, 161104 (2017).

[102] N.-B. Zhang and B.-A. Li, Impact of the nuclear equation of state on the formation of twin stars, *Eur. Phys. J. A* **61**, 31 (2025).

[103] P. Jakobus, A. Motornenko, R. O. Gomes, J. Dexheimer, and H. Stoecker, The possibility of twin star solutions in a model based on lattice QCD thermodynamics, *Eur. Phys. J. C* **81**, 41 (2021).

[104] Z. Sharifi, M. Bigdeli, and D. Alvarez-Castillo, Studying VLOCV twin compact stars with binary mergers, *Phys. Rev. D* **103**, 103011 (2021).

[105] D. Sen, N. Alam, and G. Chaudhuri, Detailed analysis of the special points on $M - R$ solutions of hybrid/twin stars, *Phys. Rev. D* **106**, 083008 (2022).

[106] P. Laskos-Patkos and Ch. C. Moustakidis, Signatures of quark deconfinement through the r -modes of twin stars, *Phys. Rev. D* **107**, 123023 (2023).

[107] E. Lope-Oter and A. Wojnar, Twin stars in General Relativity and Extended Theories of Gravity, *J. Cosmol. Astropart. Phys.* **2025** (01), 054.

[108] D. Zhou, Dwarf (Twin) Neutron Stars I: Did GW170817 Involve One? (2023), arXiv:2307.13810 [astro-ph].

[109] T. Zhou and C. Huang, Hidden Twin Star Solutions from an Agnostic Speed-of-Sound Model: Confronting XTE J1814-338's Extreme Compactness (2025), arXiv:2504.08662 [astro-ph].

[110] Z. Yang, T. Zeng, Y. Yan, W.-L. Yuan, C. Zhang, and E. Zhou, Hybrid Quark Stars with Quark-Quark Phase Transitions (2025), arXiv:2507.00776 [astro-ph].

[111] P. Laskos-Patkos, P. S. Koliogiannis, and Ch. C. Moustakidis, Hybrid stars in light of the HESS J1731-347 remnant and the PREX-II experiment, *Phys. Rev. D* **109**, 063017 (2024).

[112] J. J. Li, A. Sedrakian, and M. Alford, Ultracompact hybrid stars consistent with multimessenger astrophysics, *Phys. Rev. D* **107**, 023018 (2023).

[113] B. K. Pradhan, D. Chatterjee, and D. E. Alvarez-Castillo, Probing hadron-quark phase transition in twin stars using f-modes, *Mon Not R Astron Soc* **531**, 4640 (2024).

[114] V. P. Gonçalves, J. C. Jiménez, and L. Lazzari, Fundamental-mode eigenfrequencies of neutral and charged twin neutron stars, *Eur. Phys. J. C* **82**, 1117 (2022).

[115] P. B. Rau and A. Sedrakian, Two first-order phase transitions in hybrid compact stars: Higher-order multiplet stars, reaction modes, and intermediate conversion speeds, *Phys. Rev. D* **107**, 103042 (2023).

[116] M. C. Rodriguez, J. C. Jiménez, and I. F. Ranea-Sandoval, Classification of g -modes for neutron stars with a strong transition: Novel universal relation including slow stable twin stars (2025), arXiv:2510.06463 [hep-ph].

[117] J. Zhu, C. Wang, C. Xia, E. Zhou, and Y. Ma, Probing phase transitions in neutron stars via the crust-core interfacial mode, *Phys. Rev. D* **107**, 083023 (2023).

[118] J. C. Jiménez, L. Lazzari, and V. P. Gonçalves, How the QCD trace anomaly behaves at the core of twin stars?, *Phys. Rev. D* **110**, 114014 (2024).

[119] A. Bhattacharyya, S. K. Ghosh, M. Hanuske, and S. Raha, Rotating twin stars and signature of quark-hadron phase transition, *Phys. Rev. C* **71**, 048801 (2005).

[120] H. Dimmelmeyer, M. Bejger, P. Haensel, and J. L. Zdunik, Dynamic migration of rotating neutron stars due to a phase transition instability, *Mon Not R Astron Soc* **396**, 2269 (2009).

[121] M. Bejger, D. Blaschke, P. Haensel, J. L. Zdunik, and M. Fortin, Consequences of a strong phase transition in the dense matter equation of state for the rotational evolution of neutron stars, *A&A* **600**, A39 (2017).

[122] R. Negreiros, C. Zhang, and R. Xu, Rotational properties of inverted hybrid stars, *Phys. Rev. D* **111**, 063026 (2025).

[123] R. O. Gomes, V. Dexheimer, S. Han, and S. Schramm, Can magnetic fields (de)stabilize twin stars?, *Mon Not R Astron Soc* **485**, 4873 (2019).

[124] H. Sotani and T. Tatsumi, Quark matter with strong magnetic field and possibility of the third family of compact stars, *Mon. Not. R. Astron. Soc.*, stx219 (2017).

[125] F. Lyra, L. Moreira, R. Negreiros, R. O. Gomes, and V. Dexheimer, Compactness in the thermal evolution of twin stars, *Phys. Rev. C* **107**, 025806 (2023).

[126] J. P. Carlomagno, G. A. Contrera, A. G. Grunfeld, and D. Blaschke, Thermal twin stars within a hybrid equation of state based on a nonlocal chiral quark model compatible with modern astrophysical observations, *Phys. Rev. D* **109**, 043050 (2024).

[127] J. P. Carlomagno, G. A. Contrera, A. G. Grunfeld, and D. Blaschke, Hybrid Isentropic Twin Stars, *Universe* **10**, 336 (2024).

[128] J. G. Martinez *et al.*, PulsarJ0453+1559: A Double Neutron Star System With A Large Mass Asymmetry, *ApJ* **812**, 143 (2015).

[129] B. Müller, A. Heger, and J. Powell, Minimum Neutron Star Mass in Neutrino-Driven Supernova Explosions,

Phys. Rev. Lett. **134**, 071403 (2025).

[130] S. Gandolfi, A. Yu. Illarionov, K. E. Schmidt, F. Pedreira, and S. Fantoni, Quantum Monte Carlo calculation of the equation of state of neutron matter, Phys. Rev. C **79**, 054005 (2009).

[131] I. Tews, T. Krüger, K. Hebeler, and A. Schwenk, Neutron Matter at Next-to-Next-to-Next-to-Leading Order in Chiral Effective Field Theory, Phys. Rev. Lett. **110**, 032504 (2013).

[132] Z. F. Seidov, The Stability of a Star with a Phase Change in General Relativity Theory, Soviet Astronomy **15**, 347 (1971).

[133] J. M. Lattimer, Neutron Star Mass and Radius Measurements, Universe **5**, 10.3390/universe5070159 (2019).

[134] J. M. Lattimer, The Nuclear Equation of State and Neutron Star Masses, Annual Review of Nuclear and Particle Science **62**, 485 (2012).

[135] R. Huxford, R. Kashyap, S. Borhanian, A. Dhani, I. Gupta, and B. S. Sathyaprakash, Accuracy of neutron star radius measurement with the next generation of terrestrial gravitational-wave observatories, Phys. Rev. D **109**, 103035 (2024).

[136] V. Doroshenko, V. Suleimanov, G. Pühlhofer, and A. Santangelo, A strangely light neutron star within a supernova remnant, Nat Astron **6**, 1444 (2022).

[137] Y. Kini *et al.*, Constraining the properties of the thermonuclear burst oscillation source XTE J1814-338 through pulse profile modelling, Monthly Notices of the Royal Astronomical Society **535**, 1507 (2024).

[138] K. Maslov, N. Yasutake, D. Blaschke, A. Ayriyan, H. Grigorian, T. Maruyama, T. Tatsumi, and D. N. Voskresensky, Hybrid equation of state with pasta phases, and third family of compact stars, Phys. Rev. C **100**, 025802 (2019).

[139] D. Blaschke and D. Alvarez-Castillo, A mixing interpolation method to mimic pasta phases in compact star matter, Eur. Phys. J. A **56**, 124 (2020).

[140] V. Abgaryan, D. Alvarez-Castillo, A. Ayriyan, D. Blaschke, and H. Grigorian, Two Novel Approaches to the Hadron-Quark Mixed Phase in Compact Stars, Universe **4**, 94 (2018).

[141] N. Yasutake, R. Lastowiecki, S. Benić, D. Blaschke, T. Maruyama, and T. Tatsumi, Finite-size effects at the hadron-quark transition and heavy hybrid stars, Phys. Rev. C **89**, 065803 (2014).

[142] H. D. Thi, T. Carreau, A. F. Fantina, and F. Gulminelli, Uncertainties in the pasta-phase properties of catalysed neutron stars, A&A **654**, A114 (2021).

[143] M. Ju, J. Hu, and H. Shen, Hadron-quark Pasta Phase in Massive Neutron Stars, ApJ **923**, 250 (2021).

[144] C. R. Harris *et al.*, Array programming with NumPy, Nature **585**, 357 (2020).

[145] P. Virtanen *et al.*, SciPy 1.0: Fundamental algorithms for scientific computing in Python, Nat Methods **17**, 261 (2020).

[146] J. D. Hunter, Matplotlib: A 2D graphics environment, Computing in Science & Engineering **9**, 90 (2007).

[147] M. Waskom, Seaborn: Statistical data visualization, JOSS **6**, 3021 (2021).

[148] T. Kluyver *et al.*, Jupyter Notebooks – a publishing format for reproducible computational workflows, in *Positioning and Power in Academic Publishing: Players, Agents and Agendas*, edited by F. Loizides and B. Schmidt (IOS Press, 2016) pp. 87–90.

[149] S. K. Lam, A. Pitrou, and S. Seibert, Numba: A LLVM-based Python JIT compiler, in *Proceedings of the Second Workshop on the LLVM Compiler Infrastructure in HPC*, LLVM '15 (Association for Computing Machinery, New York, NY, USA, 2015) pp. 1–6.

[150] G. Bradski, The OpenCV Library, Dr. Dobb's Journal of Software Tools (2000).